

Molecular Dynamics Simulation Study of a Pulmonary Surfactant Film Interacting with a Carbonaceous Nanoparticle

Seungho Choe,* Rakwoo Chang,[†] Jonggu Jeon,[‡] and Angela Violi*

*Department of Mechanical Engineering, University of Michigan, Ann Arbor, Michigan; [†]Department of Chemistry, Kwangwoon University, Seoul, Republic of Korea; and [‡]Department of Chemistry, Korea University, Seoul, Republic of Korea

ABSTRACT This article reports an all-atom molecular dynamics simulation to study a model pulmonary surfactant film interacting with a carbonaceous nanoparticle. The pulmonary surfactant is modeled as a dipalmitoylphosphatidylcholine monolayer with a peptide consisting of the first 25 residues from surfactant protein B. The nanoparticle model with a chemical formula $C_{188}H_{53}$ was generated using a computational code for combustion conditions. The nanoparticle has a carbon cage structure reminiscent of the buckyballs with open ends. A series of molecular-scale structural and dynamical properties of the surfactant film in the absence and presence of nanoparticle are analyzed, including radial distribution functions, mean-square displacements of lipids and nanoparticle, chain tilt angle, and the surfactant protein B peptide helix tilt angle. The results show that the nanoparticle affects the structure and packing of the lipids and peptide in the film, and it appears that the nanoparticle and peptide repel each other. The ability of the nanoparticle to translocate the surfactant film is one of the most important predictions of this study. The potential of mean force for dragging the particle through the film provides such information. The reported potential of mean force suggests that the nanoparticle can easily penetrate the monolayer but further translocation to the water phase is energetically prohibitive. The implication is that nanoparticles can interact with the lung surfactant, as supported by recent experimental data by Bakshi et al.

INTRODUCTION

The process of combustion is, at this time, the dominant pathway through which mankind continuously injects particulate matter into the atmosphere. These combustion-generated particles are produced not only in very large amounts, but, at the smallest scale, in the form of clusters with nanometric dimensions. Modern diesel engines are a major source of these combustion-generated nanoparticles. Although the total mass of particulate emissions has been significantly reduced with the improvement of combustion efficiency and emissions control systems, the very small nanoparticles are exceedingly difficult to control by the emission systems typically installed on vehicles. In addition, the current emission regulations are mass-based and do not address the presence of nanoparticles. In fact, studies conducted on exhaust measurements of particle size and number concentration data from diesel engines (1–5) show that nanoparticles represent only 0.1–1.5% of particle volume (mass) but 35–97% of the particle number (6). Environmental regulations of diesel engines and other combustion sources based on particle mass or volume instead of particle number will nearly entirely miss the dangerous nanoparticle component of such emissions. For example, currently U.S. Environmental Protection Agency and European Union regulations on diesel engines will control particle sizes down to $2.5\ \mu\text{m}$, fully two to three orders of magnitude larger than the dimension of the nanoparticles that have been experimentally shown to dominate the diesel par-

ticle number emissions profile. (Particle mass, rather than number, is the basis for the new diesel regulations). Given that such great quantities of carbonaceous nanoparticles are being introduced into the atmosphere by combustion sources, the question naturally arises as to their environmental fate. The most direct and serious risk would seem to be the direct absorption of these particles into living human and animal systems through the process of respiration, especially in more urban environments (7). Recent studies on the mechanisms by which ultrafine particles act on biological systems reveal that particle deposition on the epithelial cells in the lungs trigger a number of responses: cell activation leading to inflammation (8–10); production of cytokines (proteins) that stimulate the release of fibrinogens, which bind to platelets, contribute to their aggregation, and enhance their ability to clot; and stimulation of nerve cells that leads to changes in the nervous system's control of breathing and heart rate (11–13). The goal of this work is therefore to explore the interactions of carbon-based nanoparticles derived from combustion sources with biomolecular structures representative of those in the lung (pulmonary surfactant) using atomistic simulations. To date, little is known about the interaction of ultrafine particles with the lung surfactant. Recent studies reported by Geiser et al. (14) and Kapp et al. (15) show that the surfactant promotes the displacement of particles from air into an aqueous subphase and the extent of particle immersion depends on the surface tension of the surfactant film. Inhaled particles, regardless of the nature of their surfaces, are submersed into the lining layer after deposition in small airways and alveoli. The displacement is promoted by the surfactant film at the air-liquid interface, whose surface tension temporarily falls to relatively low values. It is important to note that Nemmar et al. (16) have

Submitted October 18, 2007, and accepted for publication June 3, 2008.

Address reprint requests to Angela Violi, Dept. of Mechanical Engineering, University of Michigan, 2350 Hayward St., Ann Arbor, MI 48109-2125. Tel.: 734-615-6448; Fax: 734-647-9379; E-mail: avioli@umich.edu.

Editor: Gregory A. Voth.

© 2008 by the Biophysical Society
0006-3495/08/11/4102/13 \$2.00

doi: 10.1529/biophysj.107.123976

shown the passage of inhaled ^{99m}Tc -carbon particles into the blood circulation in humans. Oberdorster et al. (17) reported the substantial translocation of inhaled ^{13}C -carbon particles into the liver after whole-body inhalation exposure of rats. In other words, the inhaled material may have the respiratory system as its target organ or the respiratory system may only be a route of entry to the body. Recently, Bakshi et al. (18) examined the potential effects of metal nanoparticles (Au NP), as a model air pollutant, on the surface activity of a semisynthetic pulmonary surfactant, dipalmitoylphosphatidylcholine/palmitoyloleoylphosphatidylglycerol/surfactant protein B (DPPC/POPG/SP-B, 70:30:1). The presence of Au NP at 3.7 mol %, 0.98 wt % (Au/phospholipids) dramatically reduced the surface activity of the surfactant system.

In this work, we report on the computational investigation of the structural and dynamic effects of combustion-generated carbon nanoparticles on a lipid monolayer using molecular dynamics (MD) simulations of atomistic molecular models. In the next section, the molecular models and computer simulation methods used in this study are described in detail. Structural, dynamical, and thermodynamical analyses are then presented. It is found that the presence of nanoparticles inside the lung surfactant influences the lipid/peptide environment.

METHODS

Molecular models

Monolayer

Pulmonary lung surfactant (LS) is a mixture of lipids and proteins, and its main biophysical function is the reduction of surface tension at the air-liquid interface. This reduction stabilizes the alveoli during expiration, when the alveolar space faces the highest compressions, and reduces the amount of work required to reexpand the lung during the next respiratory cycle (19–22). LS consists of ~90% lipids (23) and 10% proteins (24,25). DPPC constitutes over 40% of the total weight of surfactant. LS works both by lowering the normal surface tension to near zero inside the lungs to reduce the work of breathing, and by stabilizing the alveoli through varying the surface tension as a function of alveolar volume (26). To accomplish this, the LS mixture must adsorb rapidly to the air-fluid interface of the alveoli after being secreted. Once at the interface, it must form a monolayer that can both achieve low surface tensions upon compression and vary the surface tension as a function of the alveolar radius. This monolayer must also be able to resist collapse under the compression that accompanies exhalation. LS also contains four lung-surfactant-specific proteins, known as SP-A, SP-B, SP-C, and SP-D. SP-A and SP-D are larger proteins thought to be responsible for the transport and recycling of LS, whereas SP-B and SP-C are smaller helical proteins believed to be important for its surface activity.

In vitro studies suggest that SP-B interacts with the headgroups of acidic surfactant lipids and enhances the adsorption, spreadability, and surface insertion of the surfactant lipids (19,24,27). In many instances, SP-B_{1–25} (the first 25 amino acids) can effectively replace the full-length SP-B (28–34). Based on previously reported MD simulation studies of LS (35,36), the model LS system used in this work is composed of DPPC along with SP-B_{1–25}, which has been demonstrated to have functions that are indispensable for LS surface activity, similar to those of full-length SP-B. In particular, we performed a series of MD simulations on a system composed of a lipid monolayer containing 90 DPPC molecules, two pulmonary SP-B_{1–25}S, ~5500 water molecules, and an appropriate number of counterions (Cl^-) to

maintain electroneutrality of the system (System I). The system is composed of two leaflets, with 45 lipids and one peptide in each leaflet. The peptide structure and coordinates were downloaded from the Protein Data Bank (code 1DFW). This latter system was then modified to allocate two identical carbonaceous nanoparticles (one nanoparticle per leaflet) to produce System II.

Nanoparticle

A combustion-generated carbon nanoparticle was produced using the AMPI (Atomistic Model for Particle Inception) code that was developed to study the transformations that occur in combustion systems during the transition from gas phase to particle inception (37). The particle has an aspect ratio close to unity, with a formula of $\text{C}_{188}\text{H}_{53}$. It has a size of ~17 Å in the longest dimension and consists of a network of five- to eight-membered fused rings resembling buckyballs. The capability of the AMPI code has been validated in different combustion conditions. Nanoparticles have been characterized in terms of chemical structure/components and relationships between structure and pathways, structure and properties, and structure and reactivity population of active sites have been addressed. In particular, computed properties of nanoparticles have been compared with experimental data in terms of H/C trends, particle morphology and depolarization ratio, and free radical concentration (38–42).

Molecular dynamics simulations

Monolayer configuration and equilibration

The initial monolayer configuration was obtained by replicating a single DPPC molecule 45 times as a monolayer in a box of size $5.0 \times 5.0 \times 20$ nm. Below the headgroup region of the monolayer, 2750 water molecules were added, and periodic boundary conditions were applied in all three directions. The TIP3P model was used for the water molecules (43,44). The second leaflet was obtained by 180° rotation of the first leaflet. The simulation box length was set to 20.0 nm in the z direction to make sure that the interaction between the system and its periodic image was minimal. A configuration made of a two-leaflet system for the monolayer simulations has been widely used in the past. Previous studies have shown that monolayer systems of several nanometers in size can reproduce most of the structural properties experimentally observed (45).

A cutoff of 1.2 nm was used for the van der Waals interactions and the particle mesh Ewald summation (46) was employed with $\kappa = 0.34 \text{ Å}^{-1}$ for electrostatic interactions. The temperature was maintained at 325 K, coupling the system to a Nose-Hoover thermostat (47), and the Langevin piston method (48) was used for pressure control. The system was equilibrated for 5 ns. The final configuration from this equilibration simulation was used as the starting condition for the next step.

Peptide insertion and equilibration

The sequence of SP-B_{1–25} in humans is FPIPL PYCWL CRALI KRIQA MIPKG. The first eight residues are highly hydrophobic and are hypothesized to form an insertion sequence, and this part of the protein is relatively inflexible due to the presence of three alternating proline residues. Residues 9–22 form an amphipathic α -helix, and the last three residues form a coil motif. A ribbon diagram of SP-B_{1–25} is shown in Fig. 1. SP-B_{1–25} was inserted into the equilibrated monolayer. The insertion was obtained by running an MD simulation with an additional hole-making force in the lipid monolayer region. After the peptide was inserted into the hole, an energy minimization step was performed. Then, an appropriate number of counterions was added to ensure electroneutrality of the system. An equilibration run of 1 ns was then performed using the $NL_z\gamma T$ ensemble, allowing the lipids to equilibrate around the peptide. The final configuration defines one of the two systems analyzed in this article, System I.

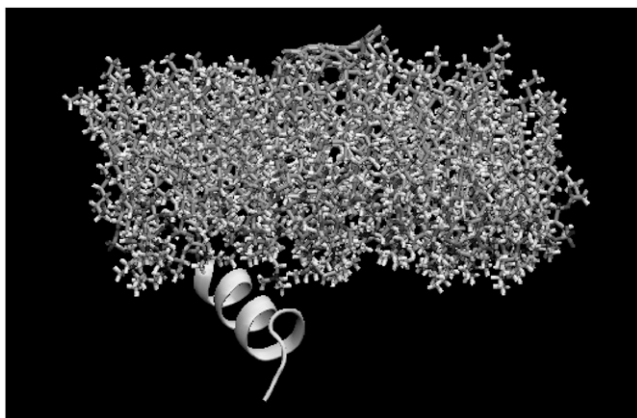


FIGURE 1 Initial setup showing one of the leaflets. Water molecules and counterions are deleted for clarity. Orange, round nanoparticles; yellow, SP-B₁₋₂₅S; other colors, DPPC lipids.

Carbonaceous nanoparticle insertion and equilibration

The nanoparticle was inserted into the equilibrated peptide + monolayer system according to a procedure similar to that described for the peptide. Every time the radius of the hole was increased, the system was minimized using the adopted-basis Newton Raphson algorithm (49). Once the nanoparticle was inserted into the hole, the system was equilibrated for 1 ns. The final configuration represents the second system of interest in this work, System II (see Fig. 2). The carbonaceous nanoparticle does not possess any electric charge or dipole, and the interactions between the nanoparticles in the two leaflets, nanoparticles and lipids or water molecules, are mainly due to the short-range van der Waals (vdW) potential. For the nanoparticle we used the aromatic carbon parameters of the CHARMM force fields.

The objective of this study is to compare Systems I and II to understand how the presence of the nanoparticle influences the main properties of the monolayer.

Simulation details

MD simulations were performed on Systems I and II in the $NL_z\gamma T$ ensemble. The surface tension of the system was kept at $\gamma = 20.0$ dyn/cm. The normal surface tension for water is 70 dyn/cm (70 nN/m), and in the lungs it is 25 dyn/cm (25 mN/m); however, at the end of the expiration, compressed surfactant phospholipid molecules decrease the surface tension to very low, near-zero levels. Pulmonary surfactant reduces surface tension, increasing compliance, which allows the lung to inflate much more easily, thereby eliminating the work of breathing. The reduction in surface tension also reduces fluid accumulation in the alveolus as the surface tension draws fluid across the alveolar wall. An additional reason to choose a surface tension of 20.0 dyn/cm was the possibility of comparing our computational results with previously obtained data (50) to validate our approach. The length of the box in the z direction (axis perpendicular to the water/lipid interface) was fixed, whereas the system could fluctuate in the x and y directions. Because the height, L_z , is constrained, the ensemble is actually $NL_zP_T T$, where P_T is the tangential pressure. In practice, one could still input an applied surface tension, and CHARMM would convert the appropriate tangential pressure. $NL_zP_T T$ was used in the potential of mean force (PMF) calculation (see below).

The $NL_z\gamma T$ ensemble was used with the Nose-Hoover thermostat and a Langevin piston of mass 500 amu with a collision frequency of 20 ps^{-1} . We set $pm_{xx} = pm_{yy} = 500$ amu, and $pm_{zz} = 0$, where pm_{xx} , pm_{yy} , and pm_{zz} are piston masses applied to the x , y , and z , directions, respectively. The simulations were carried out at 325 K. The SHAKE algorithm was utilized to hold all hydrogen bonds fixed. The simulations were run for 7 ns (5 ns), with a time step of 1 fs for System I (System II). The coordinates were saved every

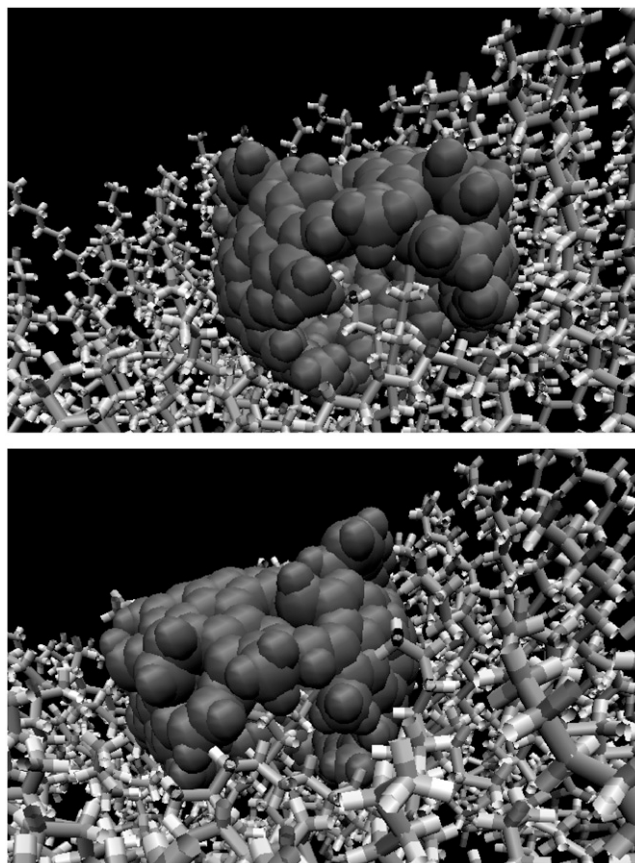


FIGURE 2 Configuration of the LS/NP system after equilibration, showing the upper leaflet (*upper*) and lower leaflet (*lower*). The particle is represented by vdW radii with red color.

1 ps to produce a trajectory with 7000 (and 5000) frames that was used for the analysis. All the simulations were carried out using CHARMM with the CHARMM27 parameter set (44,49) and VMD (51) for visualizations.

The finite size effect is not significant in these systems as described by Chang and Violi (52), since the lateral dimension of the monolayer is ~ 3 times bigger than the nanoparticle size. In addition, it has been shown that an appropriate distance between the solute protein and a simulation box boundary corresponding to ~ 4 –5 layers of lipid molecules makes it possible to neglect the size effect (53). Systems I and II fulfill these criteria, having a similar number of lipid layers between the nanoparticle and the box boundary.

Potential of mean force calculation

The PMF associated with the nanoparticle translocation across the monolayer has been calculated with the umbrella sampling technique (54) and weighted histogram analysis method (55). The reaction coordinate of the PMF was defined separately for each nanoparticle-monolayer pair. Specifically, they are given as the normal distance between the center of mass of a nanoparticle and its nearest monolayer, as follows

$$\xi_{1,2} = \pm(z_{1,2}^{\text{NP}} - z_{1,2}^{\text{M}}), \quad (1)$$

where $z_{1,2}^{\text{NP}}$ is the z coordinate of the center of mass of nanoparticles 1 and 2, respectively, and $z_{1,2}^{\text{M}}$ is the corresponding quantity for monolayers 1 and 2. The + and – in the \pm sign on the righthand side of Eq. 1 are for subscripts 1 and 2, respectively. Since the two monolayers are well separated by the water phase, ξ_1 and ξ_2 are expected to represent two independent nanoparticle translocation events. According to this definition, the nanoparticle is

located in vacuum just outside of the monolayer at $\xi \approx 21$ Å and it begins to be exposed to the water phase at $\xi < -5$ Å.

For the PMF calculation, aforementioned System I (monolayer-peptide-water) was taken and two nanoparticles were placed in vacuum, ~ 2 Å above the upper monolayer and below the lower one, respectively. The system was then equilibrated for 0.5 ns under constant *NPT* conditions ($P = 1$ bar, $T = 325$ K) (47), with harmonic restraints on nanoparticle atomic positions and the centers of mass of two monolayers. Further equilibration was performed for 1.25 ns with restraints on the center of mass of each nanoparticle.

From this, the initial configuration for each sampling window was prepared by gradually moving the restraining centers of nanoparticles at a rate of 1.25 Å/ns across the membrane. It took >30 ns to prepare the various configurations at different positions in the system. To cover most of the translocation event, the position analyzed ranged between -9.5 and 26.25 Å. These initial configurations were then used for umbrella sampling in 144 windows spanning the above range of ξ , each separated by 0.25 Å. A harmonic umbrella potential was employed with a force constant of 100 kcal/(mol \cdot Å²) and each window was sampled for 1 ns. Only the last 0.75-ns portion of the samples was used in the PMF calculation, and the convergence of PMF was monitored using PMFs from three 0.25-ns subblocks.

During the sampling, the system pressure was maintained at -18.7 bar in the x and y directions. This target lateral pressure was chosen to yield the surface tension of 20 dyn/cm assuming the normal pressure is 1 bar. The system height was kept constant by setting the Langevin piston parameter in that direction to zero. Although the normal pressure in the z direction was not controlled directly, the surface tension of the system remained close to 20 dyn/cm, indicating that the presence of vacuum region renders the normal pressure close to 1 bar. For the sampling, the CHARMM code had to be slightly modified because Eq. 1. involves only z components.

RESULTS AND DISCUSSION

Surface area

The area/lipid molecule is often used to monitor the system equilibration during a simulation run and, hence, to assess the validity of the simulation itself. Fig. 3 shows the time evolution of the area/lipid in Systems I and II. System II, which includes the nanoparticle, shows a stable surface area during the 5-ns simulation, with an average value of 59.8 ± 0.6 Å²/lipid. The value of the area is obtained by dividing the total

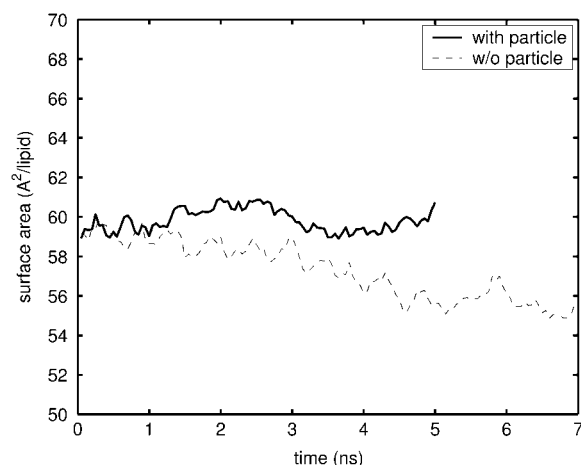


FIGURE 3 Evolution of the surface area (Å²/lipid) over time for System I, without the particle (*dashed line*), and System II, with the nanoparticle (*solid line*).

surface area by the number of lipids. The monolayer without the particle, System I, is stable between 5 and 7 ns. The average surface area during the last 2 ns is 55.6 ± 0.6 Å²/lipid, agreeing well with results obtained by Skibinsky et al. (50) from previous MD simulations (for a pure DPPC and $\gamma = 17.1$ dyn/cm at $T = 323$ K).

A larger value of the surface area for System II compared with System I is not surprising because of the presence of the nanoparticle. The value of the surface area of the particle is ~ 5 Å²/lipid (radius ~ 8 Å), so the computed surface area/lipids of ~ 60 Å² for System II seems reasonable. As can be noted from Fig. 3, the presence of the nanoparticle has a small effect on the area/lipid.

Radial distribution functions

Two different orientations of particles were considered in this work. After identifying three carbons in the cavity of the nanoparticle and connecting them to define a plane, we characterized the orientation angle as the angle between the outward vector normal to the plane and the monolayer normal (the z direction) (see Fig. 4). Fig. 5 shows the change of the orientation angle as a function of simulation time. The initial

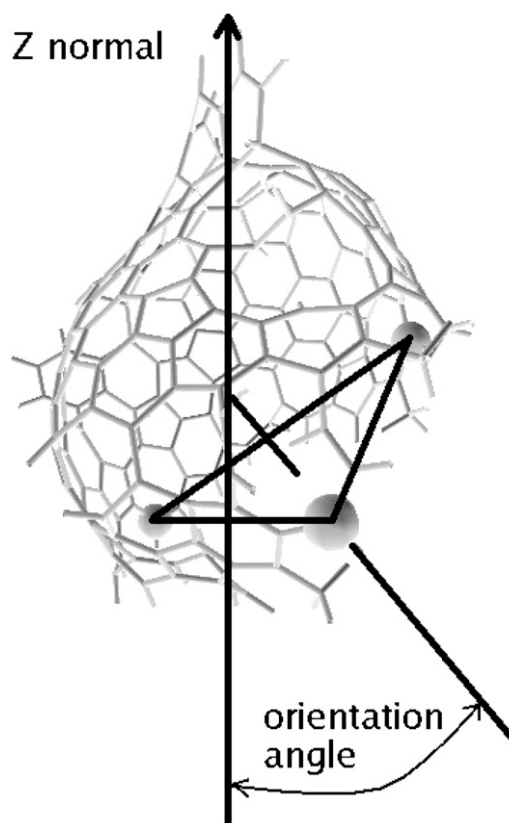


FIGURE 4 Definition of the orientation angle for the nanoparticle. After identifying three carbons in the cavity of the nanoparticle and connecting them to define a plane, the orientation angle is defined as the angle between the outward vector normal to the plane and the monolayer normal (the z direction).

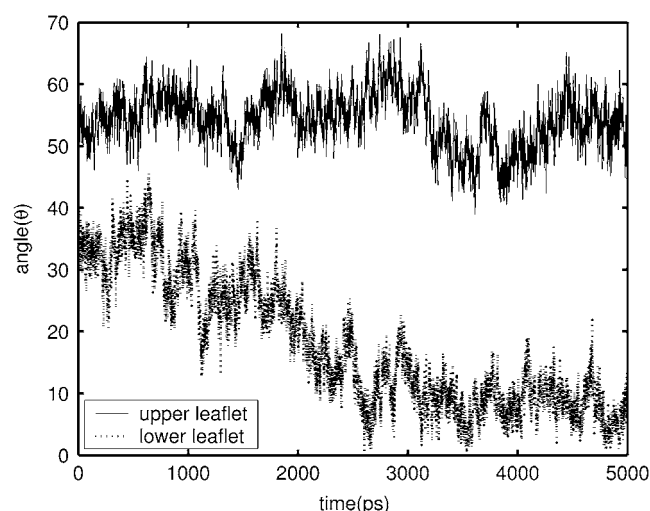


FIGURE 5 Change of the nanoparticle orientation angle as a function of simulation time. The nanoparticle with an initial angle of $\sim 55^\circ$ (System II, upper leaflet) oscillates around this value, whereas the particle with an initial angle of 35° (System II, lower leaflet) reaches a value of 10° after only 2.5 ns.

orientations of the particles were the same in the two leaflets, but their final values changed after the minimization, heating, and equilibration steps. In System II, the nanoparticle with an initial angle of $\sim 55^\circ$ (Fig. 5, *upper leaflet*) oscillates around this value, whereas the particle with an initial angle of 35° (Fig. 5, *lower leaflet*) reaches a value of 10° after only 2.5 ns.

The radial-distribution functions (RDFs), denoted as $g(r)$, give information on the probability of finding two molecules at a mutual distance, r , once geometric and density factors have been scaled out. Fig. 6 (*upper*), shows the RDFs between the tails of the lipids (the last CH_3 in the chain) and the center of mass of the nanoparticle in the upper and lower leaflets. Since the two curves look very similar, the particle orientation does not influence the interactions between the lipids and the particle itself. The first two peaks for $r < 5 \text{ \AA}$ are due to the presence of the lipid tails inside the cavity of the nanoparticles. No coating or wrapping of the lipids around the nanoparticles has been detected, since the RDFs show a third peak at a distance of $r \approx 11 \text{ \AA}$, much greater than the radius of the particle.

Fig. 6 (*lower*), reports the RDFs between the phosphorus (P) in the headgroup of lipids and the center of mass of the nanoparticle for the upper and lower leaflets in System II. The orientation in this case has an influence on the RDFs.

To determine whether this is due to the position of the nanoparticle or to its orientation, we analyzed the change of position of the center of mass of the particle over time (see Fig. 7). The two curves appear to be very similar, and hence the position of the nanoparticle does not explain the difference in RDFs. The different orientations of the nanoparticle can instead justify the difference reported in Fig. 6 (*lower*). The presence of the nanoparticle perturbs the local lipid density by pushing the neighboring lipid molecules away from the nanoparticle, which was also shown by Chang and Violi (52).

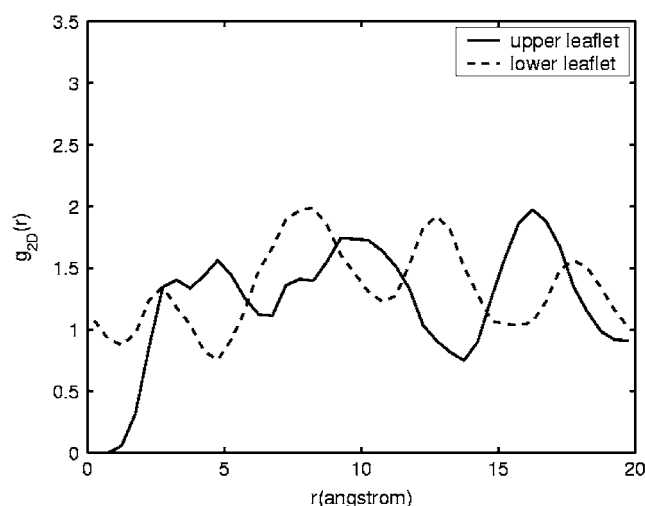
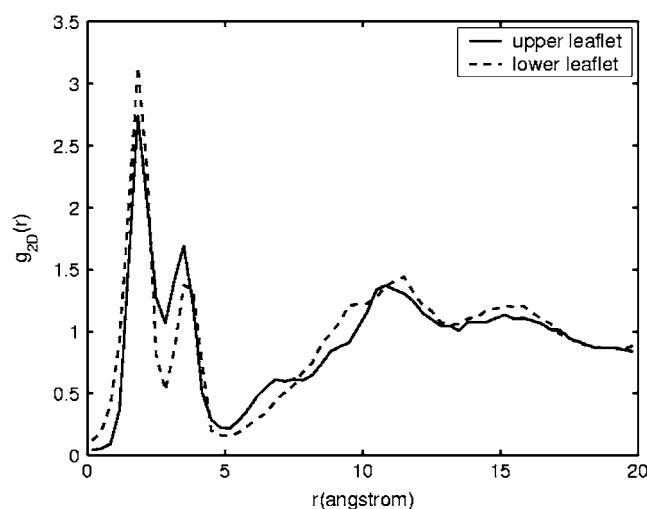


FIGURE 6 Two-dimensional radial distribution functions, g_{2D} , of the lipid tails (*upper*) and the headgroup (P) (*lower*) around the nanoparticle.

This behavior is clearly observed in the additional simulations described in Supplementary Material (Data S1), in which the nanoparticle is located initially above the lipid molecules and then reaches the lipids during the equilibration stage.

Mean-square displacement and diffusion

Fig. 8 shows the mean-square displacement (MSD) of the center of mass of a single DPPC lipid and the nanoparticle in the directions parallel ($\langle \Delta R_x^2 + \Delta R_y^2 \rangle / 4 \equiv \langle \Delta R_{\text{lateral}}^2 \rangle / 4$) and normal ($\langle \Delta R_z^2 \rangle / 2 \equiv \langle \Delta R_{\text{normal}}^2 \rangle / 2$) to the monolayer. The MSD results were averaged over the two leaflets. We show only 2 ns MSD from System II.

Initially, lateral diffusion of the single lipid is similar to that of the nanoparticle, but as the simulation proceeds, the nanoparticle reaches lower values compared to the lipid. We infer that this might be due to the presence of lipids inside the nanoparticle that hinder the motion of the particle. The same effect is obtained for normal diffusion of the nanoparticle

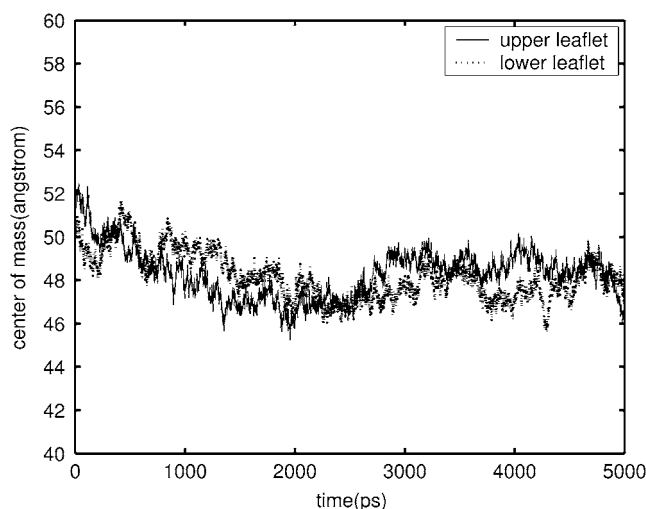


FIGURE 7 Evolution of the position of the center of mass of the nanoparticle over time, showing the z component only.

when compared with that of the single lipid. It is interesting to note that normal diffusion of the nanoparticle is significantly smaller than that of single lipids, whereas lateral diffusion is similar. A similar behavior was already reported by Chang and Violi (52), who found that the slowdown of the round nanoparticle in the normal direction results from its heavy mass. The normal diffusion clearly shows that a lipid molecule and a nanoparticle are confined to local ranges of z after 1.7 or 1.8 ns. Confinement of the nanoparticle in the normal direction can be seen in Fig. 7.

Schram and Hall reported that at all temperatures, diffusion in surfactant lipids becomes slower with surfactant proteins SP-B and SP-C, and the diffusion coefficient of the single lipid is $\sim 1.5 \times 10^{-3} \text{ \AA}^2/\text{ps}$ (56). The diffusion coefficient can be obtained from the slope of the corresponding

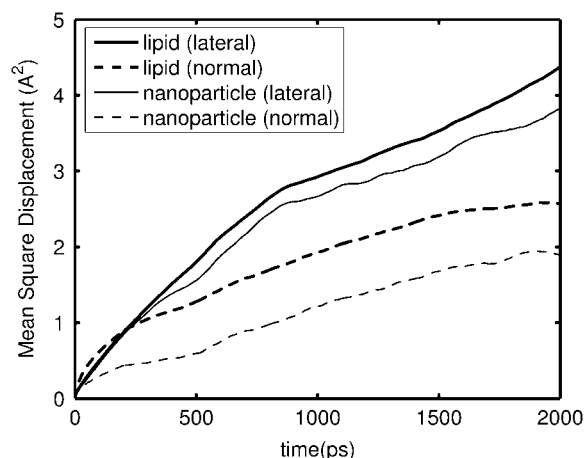


FIGURE 8 MSDs of a single DPPC lipid (thick solid line, $\langle \Delta R_{\text{lateral}}^2 \rangle / 4$; thick dashed line, $\langle \Delta R_{\text{normal}}^2 \rangle / 2$), and the round nanoparticle (thin solid line, $\langle \Delta R_{\text{lateral}}^2 \rangle / 4$; thin dashed line, $\langle \Delta R_{\text{normal}}^2 \rangle / 2$) from System II.

MSD curve. In our simulations, however, it is clear that the Brownian regime has not been reached, because the MSDs versus time are not linear. It is therefore not possible to use the Einstein relation to extract diffusion constants. Long-time diffusion of single lipids is usually slower than short-time diffusion. Compared to the experimental value (56) obtained from the long-time scale diffusion, the magnitude of lateral diffusion from our short-time scale simulations seems to confirm this. It is known that there are two regimes for lateral diffusion, i.e., short-time free volume displacements and long-time lipid motion (57–60). In Wohlt and Edholm (60), it was shown that in a first stage occurring at short times, $t < 5$ ns, the center of the lipid moves due to conformational changes of the chains, whereas the headgroup position remains relatively fixed.

Order parameters S_{CH} and S_{CC}

Another interesting property for the systems analyzed in this work is the C-H bond order parameter, S_{CH} , which can be compared to the carbon-deuterium order parameter, S_{CD} , from NMR measurements, and which is a measure of the chain behavior. In MD simulations, the order parameter S_{CH} can be obtained for the n th carbon in the chain using the expression (61)

$$S_{\text{CH}}^n = \frac{2}{3} S_{\text{xx}}^n + \frac{1}{3} S_{\text{yy}}^n, \quad (2)$$

where $S_{ij} = \langle 3\cos\theta_i\cos\theta_j - \delta_{ij} \rangle / 2$ (θ_i is the angle between the i th molecular axis and the monolayer normal (z axis)). Fig. 9 (upper) shows the values of S_{CH} averaged over the different chains in the monolayer and over the two leaflets. System I is more condensed than System II, and thus the chain results are more ordered. The computed results for System I agree well with previously published experiments (62), as well as computer simulations (63), where the values obtained for S_{CH} were $55 \text{ \AA}^2/\text{lipid}$ and $60 \text{ \AA}^2/\text{lipid}$ for DPPC and dipalmitoylphosphatidylglycerol monolayers, respectively. It is experimentally challenging to quantify the conformational order in monolayers because NMR and infrared spectroscopy may not be sufficiently sensitive. Using infrared reflection-absorption spectroscopy, Gericke et al. (62) reported that for DPPC monolayers, the region near the headgroup is more ordered than the region at the tail end, and that compression results in increased ordering. Our simulation results are in agreement with the experimental observations, and others have already confirmed this in previous MD simulations (63).

Morrow et al. (64) and Dico et al. (65) reported that for protein concentrations up to 11% (w/w), SP-B perturbs DPPC chain order only slightly in the liquid-crystalline phase. It has also been found that SP-B/C (a mixture of the two hydrophobic surfactant proteins) appears to have little or only a slight ordering effect on the PC component (66). Thus, we compared the computed chain order with data from the neat monolayer (62). Note that the protein concentration in

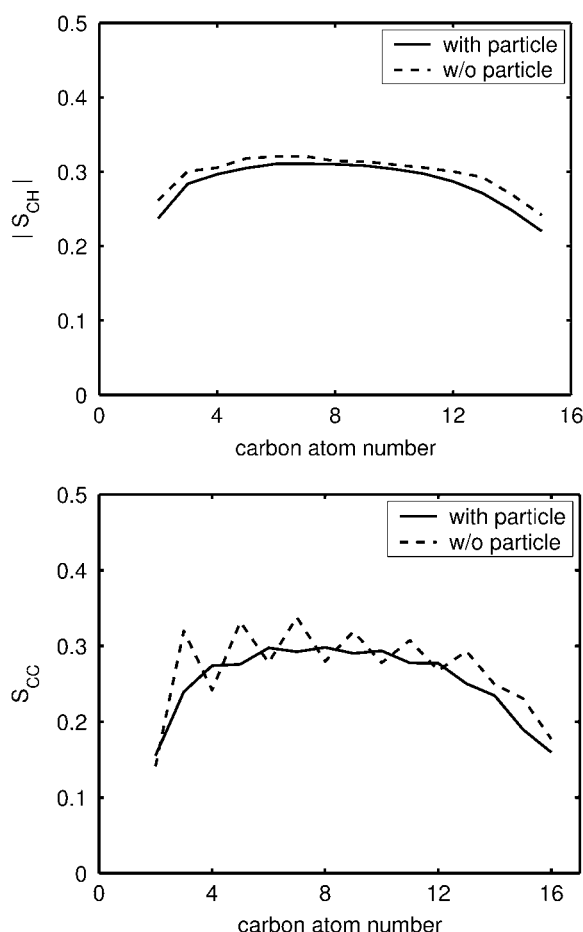


FIGURE 9 Order parameter $|S_{CH}|$ (upper) and S_{CC} (lower) averaged over the different chains in the monolayer and over the two leaflets. System I (w/o particle) is more condensed than System II (with particle) and thus the chain results are more ordered.

our system is <11% (w/w) (<9% (w/w)). In fact, the variation of the chain order depends on the concentration of SP-B. Using ^2H NMR spectra, Morrow et al. reported that the chain order was changed significantly in the presence of 15% SP-B (67). In our simulations, the total average values for S_{CH} along the chain are 0.30 and 0.28 for Systems I and II, respectively. The value of 0.30 for System I is slightly larger than values found in previous MD simulations for pure DPPC monolayers (63,68). Note that the order parameters also depend on temperature, surface area/lipid, and hydration level, and these factors could justify the discrepancy.

Recently, it has been shown that additional information about the chain conformation can be obtained by computing the carbon-carbon order parameter, S_{CC} , (69,70) as follows:

$$S_{CC} = \frac{1}{2} \langle 3 \cos^2(\phi_n) - 1 \rangle, \quad (3)$$

where ϕ_n is the angle between the normal of the monolayer and the bond connecting carbon atoms C_{n-1} and C_n . The S_{CC} order parameter formalism is of great interest for understand-

ing the conformational properties of acyl chains. It makes possible the calculation of conformer probabilities and acyl chain length, and in combination with neutron scattering experiments, it provides information about protrusion of lipids in the membrane (70). Fig. 9 (lower) shows the S_{CC} averaged over the two chains of the lipid and over the two leaflets of the monolayer. In System I, we can clearly see the difference between the odd and even order parameters, the so-called odd-even effect (71). In System II, the odd-even effect becomes smaller, and the even order parameter is larger than the odd one. The total averages along the chain are 0.27 and 0.25 for Systems I and II, respectively.

Moreover, the S_{CC} order profile may reveal an odd-even effect that cannot be observed for S_{CH} measured from deuterated chains. The S_{CC} order parameter profiles exhibit an odd-even effect especially for positions near the polar head. This effect might be a consequence of the average bent conformation of the beginning of the chain. In our calculations, this effect occurs at the beginning of the chain and is less evident after position 13. This could mean that the average orientation of the chain is tilted with respect to the z direction.

Toward the end of the chain, the S_{CC} and S_{CH} profiles are similar, accounting for the increase in conformational freedom. This odd-even effect has already been observed on *sn*-2 DLPC, DMPC, and DPPC (69) palmitic acid and on *sn*-1 DMPC chains (70).

Fig. S1 in the Supplementary Material (Data S1) shows S_{CH} and S_{CC} for each leaflet in System I. The lipids in the upper leaflet are slightly more ordered than those in the lower leaflet. This suggests that the orientation of the nanoparticle could change the order parameters, but the amount is very small in our simulations.

Chain tilt angle

The chain tilt angle is defined as the angle between the monolayer normal and the tilt vector, which is drawn from the center of the first and second carbons to the center of the 13th and 14th carbons in the chain of DPPC lipid molecules. The most probable tilt angle is $\sim 20^\circ$ for both systems, as reported in Fig. 10 (upper). The average values of the angle are $24.6 \pm 8.8^\circ$ and $24.6 \pm 7.5^\circ$ for Systems I and II, respectively. The results do not show an influence of the nanoparticle on the chain tilt angle.

Bringezu et al. reported the chain tilt angle as a function of the surface pressure, and at a pressure of 40 mN/m, the chain tilt angles were $10 \pm 1^\circ$ (M2) and $15 \pm 1^\circ$ (M3), respectively (34). Here, M2 is a mixture of DPPC/POPG/PA + SP-B₁₋₇₈, and M3 is a mixture of DPPC/POPG/PA + dSP-B₁₋₂₅. According to Table 1 of Bringezu et al. (34), SP-B₁₋₇₈ has only a slight effect on the chain tilt angle for the DPPC/POPG/PA mixture over the whole surface pressure range. It is interesting to note that the tilt angle computed from our simulations is in good agreement with the values reported from

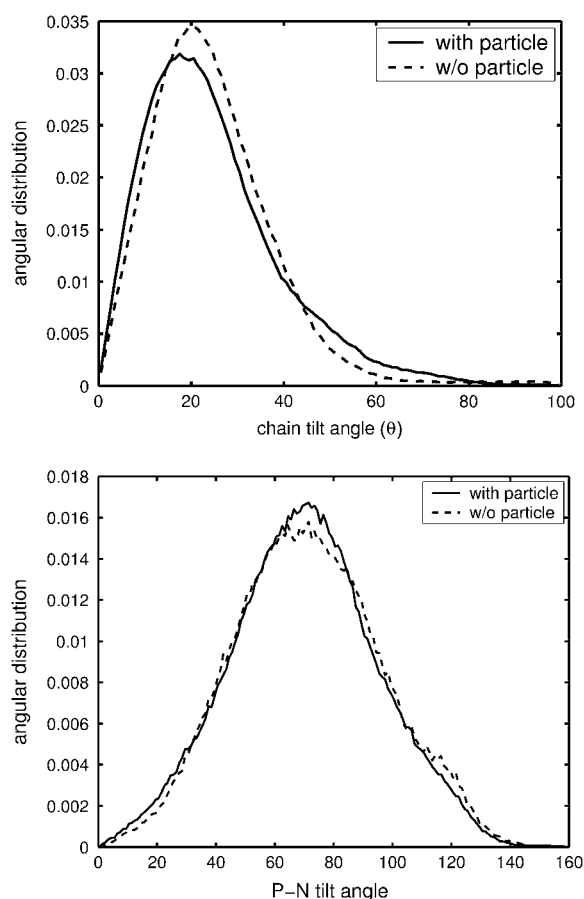


FIGURE 10 Angular distribution of the chain tilt angle (*upper*) and the P-N tilt angle (*lower*).

experiments (72–74), as well as with those obtained from computer simulations (68) on pure DPPC lipids.

On the other hand, Gericke et al. reported that the acyl chain tilt angle of DPPC decreased from $\sim 26^\circ$ in pure lipid monolayers to $\sim 10^\circ$ in the mixed monolayer films (DPPC/SP-C) using the external infrared reflection-absorption spectroscopy (75).

Choline headgroup dipole (P-N) orientation

For the DPPC monolayer, using surface potential measurements, it has been suggested that the headgroup orientation is parallel to the air-water interface (76), and in a previous simulation, the average angle between the water surface and the P-N dipole was determined to be 5° (68).

The P-N tilt angle is defined in this article as the angle between the P-N vector and the monolayer normal. The interaction between the P-N dipole and the external perturbing surface charges causes the headgroup to tilt toward or away from the monolayer, depending on the sign of the net surface charge. The headgroup tilts toward the water phase (toward the monolayer normal) in the presence of a positive surface charge. In the presence of a negative surface charge, the

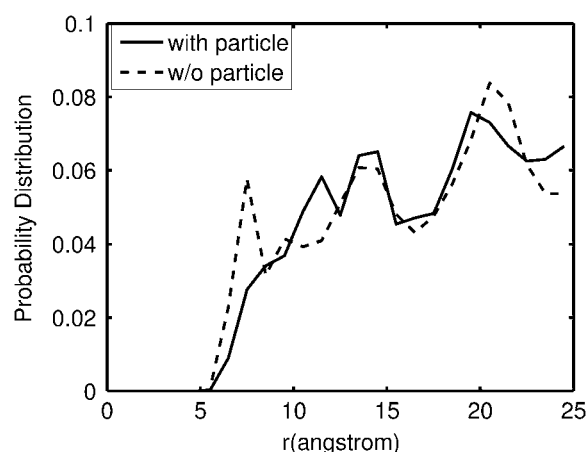


FIGURE 11 Probability distribution of the headgroup (P) around the center of mass of the N-terminal tail (residues 1–9).

headgroup tilts toward the monolayer interior (away from monolayer normal). Since SP-B_{1–25} has a positive net charge, the P-N tilt angle should be $<90^\circ$ – 95° , which was the value range obtained for pure DPPC lipids.

Our simulations show an angle of $\sim 70^\circ$ for the two systems (Fig. 10 (*lower*)). The average angle is $71.4 \pm 17.3^\circ$ for System I and $70.1 \pm 18.3^\circ$ for System II. This result suggests that the presence of the nanoparticle does not change the P-N tilt angle, as is expected, since the nanoparticle is neutral and has no dipole moment.

Helix tilt angle

The preferred conformation of the SP-B_{1–25} peptide in various lipid environments is still the subject of many studies. Several experimental measurements (77,78) and computer simulations (35,36,79,80) have been reported in the literature. To our knowledge, Frietes et al. (35) performed the only simulation that attempted a direct comparison with experimental data (x-ray scattering).

In our system, the nanoparticle interacts with the lipid molecules as well as with SP-B_{1–25}. It is therefore interesting to get insights into the interactions between the nanoparticle and the SP-B_{1–25} by computing the helix tilt angle. To define the helix tilt angle, we use the same coordinate system proposed by Choe and Sun (81). First, we define a center of mass using three C α s, e.g., using C α s in residues 10–12, 14–16, and 18–20. We named them c_1 , c_2 , and c_3 , respectively. Next, \mathbf{t}_1 and \mathbf{t}_2 are defined by connecting each center of mass: $\mathbf{t}_1 = \overrightarrow{c_1c_2}$ and $\mathbf{t}_2 = \overrightarrow{c_1c_3}$. Two different schemes are used in this article. In Scheme I, the helix tilt angle is defined as the angle between \mathbf{t}_2 and the monolayer normal, and in Scheme II, the helix tilt angle is the angle between the average of two vectors $(\mathbf{t}_1 + \mathbf{t}_2)/2$ and the monolayer normal. Note that we averaged the tilt angles over two SP-B_{1–25} peptides. In System I, the average helix tilt angles are $52.1 \pm 9.1^\circ$ and $50.2 \pm 8.9^\circ$ from Schemes I and II, respectively. These values are similar to

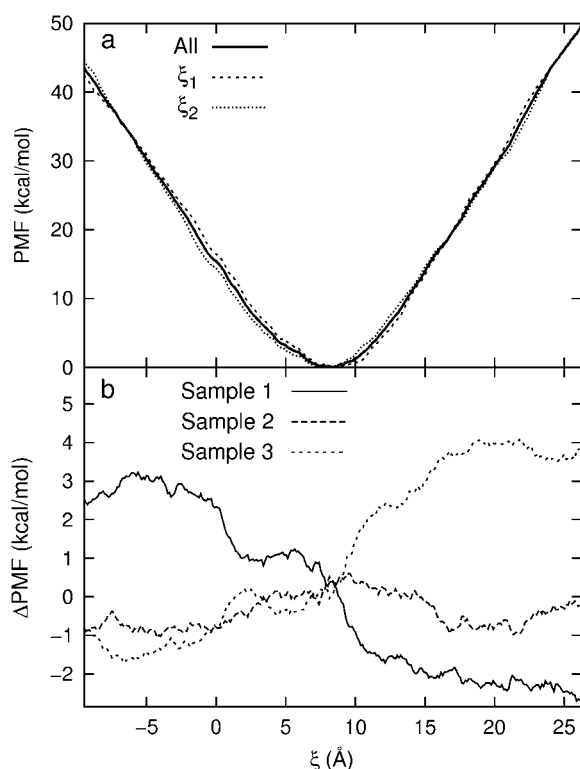


FIGURE 12 Potential of mean force (PMF) for nanoparticle translocation across the monolayer. (a) The PMF obtained from the upper (ξ_1) and lower (ξ_2) monolayer-nanoparticle pair and from the combined samples ("All") are displayed. A large value of ξ corresponds to a nanoparticle in the vacuum phase and a small ξ to a nanoparticle in the water phase. The PMF calculation was performed using the last 0.75-ns portion of the 1-ns long sample. (b) PMF from three 0.25-ns long samples (Sample 1, 0.25–0.5 ns; Sample 2, 0.5–0.75 ns; Sample 3, 0.75–1.0 ns) are shown after subtracting the PMF from the combined sample (All).

those reported in the literature. The peptide is initially tilted by $\sim 45^\circ$ with respect to the normal. In the presence of the nanoparticle (System II), the average helix tilt angle becomes smaller, $31.0 \pm 5.4^\circ$ and $30.8 \pm 6.2^\circ$ from Schemes I and II, respectively. The nanoparticle pushes the peptide away from the interface by almost 20° (System I and System II). This might suggest that the two hydrophobic molecules (the nanoparticle and the SP-B_{1–25}) repel each other.

The helix tilt angle could also be affected by the orientation of the nanoparticle. Although the average helix tilt angle over the two leaflets is $\sim 30^\circ$, the tilt angle of the two SP-B_{1–25} peptides in each leaflet is different. The tilt angles are $21.2 \pm 9.1^\circ$ and $40.5 \pm 8.2^\circ$ for the upper and lower leaflets, respectively.

The different angles are a consequence of the different interactions of the nanoparticle with the headgroup shown in Fig. 6 (lower), in the two leaflets. In Fig. 6 (lower), the nanoparticle in the upper leaflet shows more repulsive interaction with the lipid headgroups. This can cause some different interactions of the headgroups with SP-B_{1–25}, and thus the helix tilt angle could be also affected and possibly affect the proper functioning of the SP-B_{1–25}.

The N-terminal tail (residues 1–9) of SP-B is particularly critical for the surface-tension-reducing property of the protein (82). Thus, the position and depth of those residues are important for SP-B (and SP-B_{1–25}) to function. Fig. 11 reports the probability distribution function of the headgroup (P) around the center of mass of those nine residues. The first peak is shifted (~ 5 Å) in the presence of the nanoparticle, and this can be further evidence that the nanoparticle can affect the interaction between the headgroup and SP-B_{1–25}. The position of the first peak in the radial distribution is also slightly dependent on the orientation of the nanoparticle (not shown), but the amount of the shift is very small, ~ 1 Å.

Potential of mean force for nanoparticle translocation

Fig. 12 shows the PMF for nanoparticle translocation across the monolayer. In Fig. 12 a, the PMF from the combination of upper and lower monolayers (ξ_1 and ξ_2 , respectively) is shown together with individual results. In Fig. 12 b, the PMFs of three 0.25-ns long subblocks (Samples 1–3) are displayed after subtracting the PMF of the entire 0.75-ns sample. The two individual PMF curves in Fig. 12 a agree with the combined PMF labeled "All" within ~ 1.5 kcal/mol. The nanoparticle penetration into the monolayer is represented by a monotonic decrease in the PMF between $\xi = 26$ Å and $\xi = 8$ Å. In particular, the nanoparticle makes contact with the monolayer from the vacuum phase at $\xi \approx 21$ Å, but it is not noticeable from the PMF. However, we note a small change in the slope of PMF at $\xi = 24$ Å, which might be indicative of the adsorption of nanoparticle on the lipids. The nanoparticle is most stable inside the monolayer at $\xi = 8$ Å, where maximum interaction between the nanoparticle and the lipid acyl chains is possible.

As the nanoparticle moves further toward the lipid headgroup region, the PMF begins to rise, and this trend continues until the nanoparticle is partially exposed to the water phase at $\xi \approx -9$ Å. Because of the limited range of the reaction coordinate, the PMF does not exhibit a plateau at either large or small ξ . Thus, it is difficult to determine the relative stability of the nanoparticle in the vacuum and water phases. However, as reported in Fig. 12 b, the PMF tends to change systematically with longer sampling. For example, the PMF from Sample 3 in Fig. 12 b (0.75–1 ns) is larger than that of the shorter samples (Fig. 12 b, Samples 1 and 2: 0.25–0.5 and 0.5–0.75 ns, respectively) in the vacuum region ($\xi > 21$ Å). On the other hand, the PMF tends to decrease at $\xi < 0$ Å with longer sampling. Thus, with longer sampling, the nanoparticle is expected to be more stable in the water than in the vacuum phase. From Fig. 12 b, we estimate the uncertainty in the PMF of Fig. 12 a as $+5$ kcal/mol in the vacuum and -2 kcal/mol in the water side.

The umbrella sampling was performed without any restraint on the nanoparticle orientation. Since the sample was initially prepared with the nanoparticle in the vacuum region,

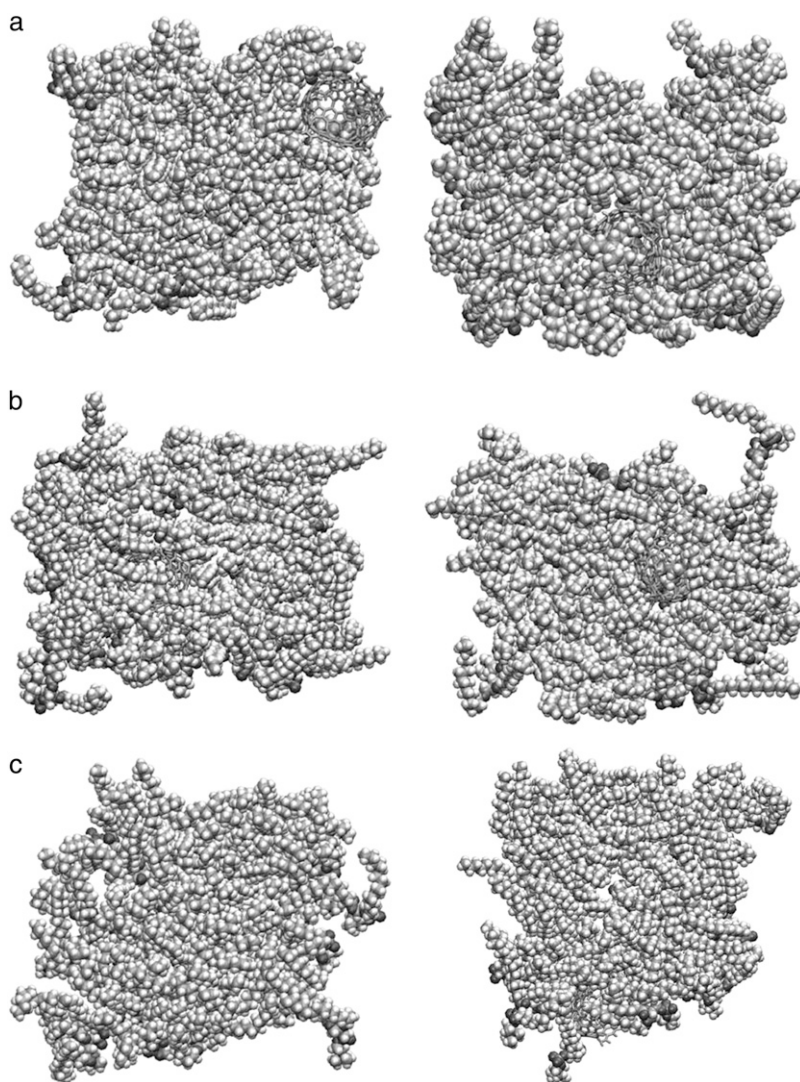


FIGURE 13 Lipid wraps its tail around the nanoparticle during the umbrella sampling. The top view on each leaflet is shown at $\xi = 0.25, -1.75$, and -9.25 Å, respectively. The lipid molecules are represented by vdW radii and the nanoparticle is colored orange (*left*, NP1; *right*, NP2). (*a*) $\xi = 0.25$ Å. The NP2 cavity is filled with two acyl chains from two different lipids. This is the earliest point at which lipids enter the cavity. (*b*) $\xi = -1.75$ Å. The NP1 cavity is filled with one acyl chain. This is where the NP1 cavity is filled with a lipid chain for the first time. (*c*) $\xi = -9.25$ Å. This is close to the end of the PMF. This shows that the NP1 and NP2 cavities are filled with two acyl chains. Note that one of them has two chains from a single lipid, whereas the other has one chain from two different lipids.

the nanoparticle was allowed to freely rotate. Inspection of the sampled configuration reveals that the nanoparticle faces the monolayer with its convex side in the region near the monolayer (data not shown). This is understandable, because this configuration is expected to maximize the attractive Lennard-Jones interaction between the nanoparticle and the lipid acyl chains. It was also found that this nanoparticle orientation is maintained during the entire translocation process. This will minimize possible entanglement of lipid acyl chains in the cavity of the nanoparticle and facilitate the movement of the nanoparticle. If the translocation had been initiated in the water phase, the nanoparticle would have assumed the reverse orientation. The sampling described here is too short to allow for nanoparticle reorientation inside the monolayer, but the above considerations indicate that this may not be a severe limitation.

A very interesting finding is the wrapping (or coating) during the umbrella sampling. The cavity of the nanoparticle begins to be filled with lipid chains at a late stage of penetration. Fig. 13 depicts the wrapping during the umbrella

sampling. Only the lipid chains enter the cavity. For NP1 (the nanoparticle in the upper leaflet), which has $\theta \approx 180^\circ$, a single lipid begins to occupy the cavity at $\xi = -1.75$ Å by wrapping its tail around the edge of the NP. For NP2 (the nanoparticle in the lower leaflet), which is oriented more sideways, this took place earlier, at $\xi = 0.25$ Å. In the end, the cavity is filled with two lipids. Similar behavior was reported for a C_{60} molecule adsorbed deeply in the bilayer (83).

CONCLUSIONS

We performed MD simulations to study the effects of the presence of a carbonaceous nanoparticle in a lung surfactant composed of DPPC and SP-B₁₋₂₅ peptides. Two systems were considered: System I, composed of DPPC, SP-B₁₋₂₅, and water; and System II, obtained by adding a nanoparticle to System I. The $NL_z\gamma T$ ensemble was used for the simulations with a surface tension of $\gamma = 20.0$ dyn/cm. We computed various properties of the systems, including the radial distribution functions, the mean-square displacements, the

order parameters (S_{CH} and S_{CC}), the chain tilt angle, the P-N orientation, the helix tilt angle, and the PMF of the permeation. It is noted that during the simulations a lipid wraps its tail around the nanoparticle, and that by the end of the simulations the cavity is filled with one or two lipids. In addition, the orientation of the nanoparticle has an influence on the lipid chain order. The nanoparticle investigated in this article is not symmetric, and the interactions with other molecules (lipids, SP-B₁₋₂₅) are also influenced by the particle orientation. The major effect of the nanoparticle on lung surfactant is the interaction between the nanoparticle and SP-B₁₋₂₅. Our simulations show that they repel each other. The PMF calculation clearly shows that carbon nanoparticles strongly adsorb in the tail region of the lung surfactant monolayer once they are inhaled. On the other hand, it is unlikely for the adsorbed nanoparticles to easily translocate into the water phase, because the free energy barrier for the nanoparticle translocation is too high to be overcome simply by thermal fluctuation, which is ~ 0.6 kcal/mol at ambient temperature. A similar behavior was also found in the previous bilayer simulations (52). It would be interesting in the future to study the PMF between SP-B₁₋₂₅ and the nanoparticle with an additional umbrella sampling.

The variation of results in the experimentally determined position and orientation of SP-B and DPPC layers suggests that there is no specificity in the interactions between SP-B and DPPC lipids. It also has been proposed that the topographical and structural organization of SP-B may depend on experimental conditions (84–87). A recent simulation showed that in DPPC monolayers, SP-B₁₋₂₅ mainly interacts with the zwitterionic lipid through hydrophobic interactions (36). Frietes et al. also suggested that both hydrophobic interactions and salt bridges are important (35). It is worth mentioning that, to date, the study described by Frietes et al. (35) is the simulation on the SP-B peptide in a lipid monolayer that has been most extensively validated experimentally. It has also been shown that the polar and cationic amino acids of the peptide form hydrogen bond interactions with headgroups of lipids, and it was suggested that these hydrogen bonds help determine the position and orientation of the peptide on the interface (79). Although the correct position and the helix tilt angle of SP-B₁₋₂₅ have not yet been established, the nanoparticle can affect the interaction between the lipids and the peptide, and it can hinder the function of lung surfactant. More quantitative analyses will be necessary to confirm these theories.

In this work, we didn't consider any radical formation or oxidation. The effect of chemically modified carbon nanoparticles on lung surfactant can be interesting. In addition, the effect of particle morphology on the surfactant is another research subject of interest.

SUPPLEMENTARY MATERIAL

To view all of the supplemental files associated with this article, visit www.biophysj.org.

The authors are grateful to Prof. Benoit Roux, Dr. Serge Crouzy, and Dr. Alan Grossfield for providing the weighted histogram analysis method (WHAM) codes.

This work was funded in part by a National Science Foundation grant (NSF-CAREER 0644639) to A.V. R.C. acknowledges support from the Korea Research Foundation Grant funded by the Korean Government (MOEHRD, Basic Research Promotion Fund) (KRF-2007-331-C00132).

REFERENCES

- Kittelson, D. B. 1998. Engines and nanoparticles: a review. *J. Aerosol Sci.* 29:575–588.
- Bagley, S. T., K. J. Baumgard, L. D. Gratz, J. H. Johnson, and D. G. Leddy. 1996. Characterization of fuel and aftertreatment device effects on diesel emissions. *Res. Rep. Health Eff. Inst.* 76:1–75.
- Ristovski, Z. D., L. Morawska, N. D. Bofinger, and J. Hitchins. 1998. Submicrometer and supermicrometer particulate emission from spark ignition vehicles. *Environ. Sci. Technol.* 32:3845–3852.
- Maricq, M. M., D. H. Podsiadlik, and R. E. Chase. 1999. Examination of the size-resolved and transient nature of motor vehicle particle emissions. *Environ. Sci. Technol.* 33:1618–1626.
- Morawska, L., N. D. Bofinger, L. Kocis, and A. Nwankwoala. 1998. Submicrometer and supermicrometer particles from diesel vehicle emissions. *Environ. Sci. Technol.* 32:2033–2042.
- Abdul-Khalek, I. S., D. B. Kittelson, B. R. Graskow, Q. Wei, and F. Brear. 1998. Diesel exhaust particle size: measurement issues and trends. *Soc. Automot. Eng.*, technical paper No. 980525.
- Oberdorster, G., J. Ferin, and B. E. Lehnert. 1994. Correlation between particle size, in vivo particle persistence, and lung injury. *Environ. Health Perspect.* 102:173–179.
- Warheit, D., B. Laurence, K. Reed, D. Roach, G. Reynolds, and T. Webb. 2004. Comparative pulmonary toxicity assessment of single-wall carbon nanotubes in rats. *Toxicol. Sci.* 77:117–125.
- Lam, C., J. James, R. McCluskey, and R. Hunter. 2004. Pulmonary toxicity of single-wall carbon nanotubes in mice 7 and 90 days after intratracheal instillation. *Toxicol. Sci.* 77:126–134.
- Schedvova, A., E. Kisin, R. Mercer, A. Murray, V. Johnson, A. Potapovich, Y. Tyurina, O. Gorelik, S. Arepalli, and D. Schwegler-Berry. 2005. Unusual inflammatory and fibrogenic pulmonary responses to single-walled carbon nanotubes in mice. *Am. J. Physiol. Lung Cell. Mol. Physiol.* 289:L698–L708.
- Mauderly, J. L. 1994. Pulmonary toxicity of inhaled diesel exhaust and carbon black in chronically exposed rats. I. Neoplastic and non-neoplastic lung lesions. *Res. Rep. Health Eff. Inst.* 68:1–75.
- Donaldson, K., R. Aitken, L. Tran, V. Stone, R. Duffin, G. Forrest, and A. Alexander. 2006. Carbon nanotubes: a review of their properties in relation to pulmonary toxicology and workplace safety. *Toxicol. Sci.* 92:5–22.
- Magrez, A., S. Kasas, V. Salicio, N. Pasquier, J. W. Seo, M. Celio, S. Catsicas, B. Schwaller, and L. Forro. 2006. Cellular toxicity of carbon-based nanomaterials. *Nano Lett.* 6:1121–1125.
- Geiser, M., S. Schurkh, and P. Gehr. 2003. Influence of surface chemistry and topography of particles on their immersion into the lungs surface-lining layer. *J. Appl. Physiol.* 94:1793–1801.
- Kapp, N., W. Kreyling, H. Schulz, V. I. Hof, P. Gehr, M. Semmler, and M. Geiser. 2004. Electron energy loss spectroscopy for analysis of inhaled ultrafine particles in rat lungs. *Microsc. Res. Tech.* 63:298–305.
- Nemmar, A., P. H. M. Hoet, B. Vanquickenborne, D. Dinsdale, M. Thomeer, M. F. Hoylaerts, H. Vanbilloen, L. Mortelmans, and B. Nemery. 2002. Passage of inhaled particles into the blood circulation in humans. *Circulation.* 105:411–414.
- Oberdorster, G., Z. Sharp, V. Atudorei, A. Elder, R. Gelein, A. Lunts, W. Kreyling, and C. Cox. 2002. Extrapulmonary translocation of ultrafine carbon particles following whole-body inhalation exposure of rats. *J. Toxicol. Environ. Health A.* 65:1531–1543.

18. Bakshi, M. S., L. Zhao, R. Smith, F. Possmayer, and N. O. Petersen. 2008. Metal nanoparticle pollutants interfere with pulmonary surfactant function in vitro. *Biophys. J.* 94:855–868.
19. Batenburg, J. J., and H. P. Haagsman. 1998. The lipids of pulmonary surfactant: dynamics and interactions with proteins. *Prog. Lipid Res.* 37:235–276.
20. Goerke, J. 1998. Pulmonary surfactant: functions and molecular composition. *Biochim. Biophys. Acta.* 1408:79–89.
21. Zasadzinski, J. A., J. Ding, H. E. Warriner, and F. Bringezu. 2001. The physics and physiology of lung surfactants. *Curr. Opin. Colloid Interface Sci.* 6:506–513.
22. Ghodrat, M. 2006. Lung surfactants. *Am. J. Health Syst. Pharm.* 63:1504–1521.
23. Veldhuizen, R., K. Nag, S. Orgeig, and F. Possmayer. 1998. The role of lipids in pulmonary surfactant. *Biochim. Biophys. Acta.* 1408:90–108.
24. Hawgood, S., M. Derrick, and F. Poulain. 1998. Structure and properties of surfactant protein B. *Biochim. Biophys. Acta.* 1408:150–160.
25. Perez-Gil, J., and K. M. W. Keough. 1998. Interfacial properties of surfactant proteins. *Biochim. Biophys. Acta.* 1408:203–217.
26. Pison, U., R. Herold, and S. Schurch. 1996. The pulmonary surfactant system: biological functions, components, physiological properties and alterations during lung disease. *Coll. Surf.* 114:165–184.
27. Johansson, J., and T. Curstedt. 1997. Molecular structures and interactions of pulmonary surfactant components. *Eur. J. Biochem.* 244:675–693.
28. Longo, M. L., A. M. Bisagno, J. A. Zasadzinski, R. Bruni, and A. J. Waring. 1993. A function of lung surfactant protein SP-B. *Science.* 261:453–456.
29. Lee, K. Y. C., M. M. Lipp, J. A. Zasadzinski, and A. J. Waring. 1997. Effects of lung surfactant protein. SP-B and model SP-B peptide on lipid monolayers at the air-water interface. *Colloids Surf. A.* 128:225–242.
30. Veldhuizen, E. J. A., A. J. Waring, F. J. Walther, J. J. Batenburg, L. M. G. van Golde, and H. P. Haagsman. 2000. Dimeric N-terminal segment of human surfactant protein B (dSP-B_{1–25}) has enhanced surface properties compared to monomeric SP-B_{1–25}. *Biophys. J.* 79:377–384.
31. Gupta, M., J. M. Hernandez-Juviel, A. J. Waring, R. Bruni, and F. J. Walther. 2000. Comparison of functional efficacy of surfactant protein B analogues in lavaged rats. *Eur. Respir. J.* 16:1129–1133.
32. Gupta, M., J. M. Hernandez-Juviel, A. J. Waring, and F. J. Walther. 2001. Function and inhibition sensitivity of the N-terminal segment of surfactant protein B (SP-B_{1–25}) in preterm rabbit. *Thorax.* 56:871–876.
33. Flanders, B. N., S. A. Vickery, and R. C. Dunn. 2002. Divergent fluctuations in the molar area of a model lung surfactant. *J. Phys. Chem. B.* 106:3530–3533.
34. Bringezu, F., J. Q. Ding, G. Brezesinski, A. J. Waring, and J. A. Zasadzinski. 2002. Influence of pulmonary surfactant protein B on model lung surfactant monolayers. *Langmuir.* 18:2319–2325.
35. Frietes, J. A., Y. Choi, and D. J. Tobias. 2003. Molecular dynamics simulations of a pulmonary surfactant protein B peptide in a lipid monolayer. *Biophys. J.* 84:2169–2180.
36. Kaznessis, Y. N., S. Kim, and R. G. Larson. 2002. Specific mode of interaction between components of model pulmonary surfactants using computer simulations. *J. Mol. Biol.* 322:569–582.
37. Violi, A. 2004. Modeling of soot particle inception in aromatic and aliphatic premixed flames. *Combust. Flame.* 139:279–287.
38. Violi, A., A. F. Sarofim, and G. A. Voth. 2004. Kinetic Monte Carlo-molecular dynamics approach to model soot inception. *Combust. Sci. Technol.* 176:991–1005.
39. Violi, A., G. A. Voth, and A. F. Sarofim. 2005. The relative roles of acetylene and aromatic precursors during soot particle inception. *Proc. Combust. Inst.* 30:1343–1351.
40. Violi, A., and A. Venkatnathan. 2006. Combustion-generated nanoparticles produced in a benzene flame: a multiscale approach. *J. Chem. Phys.* 125:0544302.
41. Izvekov, S., and A. Violi. 2006. A coarse-grained molecular dynamics study of carbon nanoparticle aggregation. *J. Chem. Theory Comput.* 2:504–512.
42. Chung, S. H., and A. Violi. 2007. Insights on the nanoparticle formation process in counterflow diffusion flames. *Carbon.* 45:2400–2410.
43. Jorgensen, W. L., J. Chandrasekhar, J. D. Madura, R. W. Impey, and M. L. Klein. 1983. Comparison of simple potential functions for simulating liquid water. *J. Chem. Phys.* 79:926–935.
44. MacKerell, A. D., D. Bashford, M. Bellott, R. L. Dunbrack, J. D. Evanseck, M. J. Field, S. Fischer, J. Gao, H. Guo, S. Ha, D. Joseph-McCarthy, L. Kuchnir, K. Kucera, F. T. K. Lau, C. Mattos, S. Michnick, T. Ngo, D. T. Nguyen, B. Prodhom, W. E. Reiher, B. Roux, M. Schlenkrich, J. C. Smith, R. Stote, J. Straub, M. Watanabe, J. Wiorkiewicz-Kuczera, D. Yin, and M. Karplus. 1998. All-atom empirical potential for molecular modeling and dynamics studies of proteins. *J. Phys. Chem. B.* 102:3586–3616.
45. Feller, S. E., Y. Zhang, and R. W. Pastor. 1995. Computer simulation of liquid/liquid interfaces. II. Surface tension-area dependence of a bilayer and monolayer. *J. Chem. Phys.* 103:10267–10276.
46. Essmann, U., L. Perera, M. L. Berkowitz, T. Darden, H. Lee, and L. G. Pedersen. 1995. A smooth particle mesh Ewald method. *J. Chem. Phys.* 103:8577–8593.
47. Hoover, W. G. 1985. Canonical dynamics: equilibrium phase-space distributions. *Phys. Rev. A.* 31:1695–1697.
48. Feller, S. E., Y. Zhang, Y. Pastor, and B. R. Brooks. 1995. Constant pressure molecular dynamics simulation: the Langevin piston method. *J. Chem. Phys.* 103:4613–4621.
49. Brooks, B. R., R. E. Bruccoleri, B. D. Olafson, and D. J. States. 1983. CHARMM: a program for macromolecular energy, minimization, and molecular dynamics calculations. *J. Comput. Chem.* 4:187–217.
50. Skibinsky, A., R. M. Venable, and R. W. Pastor. 2005. A molecular dynamics study of the response of lipid bilayers and monolayers to trehalose. *Biophys. J.* 89:4111–4121.
51. Humphrey, W., A. Dalke, and K. Schulten. 1996. VMD: visual molecular dynamics. *J. Mol. Graph.* 14:33–38.
52. Chang, R., and A. Violi. 2006. Insights into the effect of combustion-generated carbon nanoparticles on biological membranes: a computer simulation. *J. Phys. Chem. B.* 110:5073–5083.
53. Weinstein, H. 2006. Hallucinogen actions on 5-HT receptors reveal distinct mechanisms of activation and signaling by G protein-coupled receptors. *AAPS J.* 7:E871–E884.
54. Torrie, G. M., and J. P. Valleau. 1977. Nonphysical sampling distributions in Monte Carlo free energy estimation: umbrella sampling. *J. Comput. Phys.* 23:187–199.
55. Kumar, S., J. M. Rosenberg, D. Bouzida, R. H. Swendsen, and P. A. Kollman. 1992. The weighted histogram analysis method for free-energy calculations on biomolecules. I. The method. *J. Comput. Chem.* 13:1011–1021.
56. Schram, V., and S. B. Hall. 2004. SP-B and SP-C alter diffusion in bilayers of pulmonary surfactant. *Biophys. J.* 86:3734–3743.
57. Vaz, W., and P. Almeida. 1991. Microscopic versus macroscopic diffusion in one-component fluid phase lipid bilayer membranes. *Biophys. J.* 60:1553–1554.
58. Ayton, G. S., and G. A. Voth. 2004. Mesoscopic lateral diffusion in lipid bilayers. *Biophys. J.* 87:3299–3311.
59. Klauda, J. B., B. R. Brooks, and R. W. Pastor. 2006. Dynamical motions of lipids and a finite size effect in simulations of bilayers. *J. Chem. Phys.* 125:144710.
60. Wohlert, J., and O. Edholm. 2006. Dynamics in atomistic simulations of phospholipid membranes: nuclear magnetic resonance relaxation rates and lateral diffusion. *J. Chem. Phys.* 125:204703.
61. Egberts, E., and H. J. C. Berendsen. 1988. Molecular dynamics simulation of a smectic liquid crystal with atomic detail. *J. Chem. Phys.* 89:3718–3732.
62. Gericke, A., D. J. Moore, R. K. Erululla, R. Bittman, and R. Mendelsohn. 1996. Partially deuterated phospholipids as infrared

- structure probes of conformational order in bulk and monolayer phases. *J. Mol. Struct.* 379:227–239.
63. Kaznessis, Y. N., S. Kim, and R. G. Larson. 2002. Simulations of zwitterionic and anionic phospholipid monolayers. *Biophys. J.* 82: 1731–1742.
 64. Morrow, M., J. Perez-Gil, G. Simatos, C. Boland, J. Stewart, D. Absolom, V. Sarin, and K. Keough. 1993. Pulmonary surfactant-associated protein SP-B has little effect on acyl chains in dipalmitoylphosphatidylcholine dispersions. *Biochemistry*. 32:4397–4402.
 65. Dico, A., J. Hancock, M. Morrow, J. Stewart, S. Harris, and K. Keough. 1997. Pulmonary surfactant protein SP-B interacts similarly with dipalmitoylphosphatidylglycerol and dipalmitoylphosphatidylcholine in phosphatidylcholine/phosphatidylglycerol mixture. *Biochemistry*. 36:4172–4177.
 66. Brockman, J. M., Z. Wang, R. H. Notter, and R. A. Dluhy. 2003. Effect of hydrophobic surfactant proteins SP-B and SP-C on binary phospholipid monolayers. II. Infrared external reflectance-absorption spectroscopy. *Biophys. J.* 84:326–340.
 67. Morrow, M. R., J. Stewart, S. Taneva, A. Dico, and K. M. W. Keough. 2004. Perturbation of DPPC bilayers by high concentration of pulmonary surfactant protein SP-B. *Eur. Biophys. J.* 33:285–290.
 68. Dominguez, H., A. M. Smondyrev, and M. L. Berkowitz. 1999. Computer simulation of phosphatidylcholine monolayers at air/water and carbontetrachloride/water interfaces. *J. Phys. Chem. B.* 103:9582–9588.
 69. Douliez, J. P., A. Leonard, and E. J. Dufourc. 1995. Restatement of order parameters in biomembranes: calculation of C–C bond order parameters from C–D quadrupolar splittings. *Biophys. J.* 68:1727–1739.
 70. Douliez, J. P., A. Ferrarini, and E. J. Dufourc. 1998. On the relationship between C–C and C–D order parameters and its use for studying the conformation of lipid acyl chains in biomembranes. *J. Chem. Phys.* 109:2513–2518.
 71. Smondyrev, A. M., and M. L. Berkowitz. 1999. Molecular dynamics study of Sn-1 and Sn-2 chain conformations in dipalmitoylphosphatidylcholine membranes. *J. Chem. Phys.* 110:3981–3985.
 72. Brauner, J. W., R. Mendelsohn, and F. G. Prendergast. 1987. Tenuated total reflectance Fourier transform infrared studies of the interaction of melittin, two fragments of melittin, and δ -hemolysin with phosphatidylcholines. *Biochemistry*. 26:8151–8158.
 73. Brezesinski, G., A. Dietrichand, B. Struth, and C. Bohm. 1995. Influence of ether linkages on the structure of double-chain phospholipid monolayers. *Chem. Phys. Lipids*. 76:145–157.
 74. Ma, G., and H. C. Allen. 2006. DPPC Langmuir monolayer at the air-water interface: probing the tail and head groups by vibrational sum frequency generation spectroscopy. *Langmuir*. 22:5341–5349.
 75. Gericke, A., C. R. Flach, and R. Mendelsohn. 1997. Structure and orientation of lung surfactant SP-C and L- α -dipalmitoylphosphatidylcholine in aqueous monolayers. *Biophys. J.* 73:492–499.
 76. Mohwald, H. 1990. Phospholipid and phospholipid-protein monolayers at the air/water interface. *Annu. Rev. Phys. Chem.* 41:441–476.
 77. Gordon, L. M., S. Horvath, M. L. Longo, J. Zasadzinski, H. W. Taesch, K. Faull, C. Leung, and A. J. Waring. 1996. Conformation and molecular topography of the N-terminal segment of surfactant protein B in structure-promoting environments. *Protein Sci.* 5:1662–1675.
 78. Lee, K. Y. C., J. Majewski, T. L. Kuhl, P. B. Howes, K. Kjaer, M. M. Lipp, A. J. Waring, J. A. Zasadzinski, and G. S. Smith. 2001. Synchrotron x-ray study of lung surfactant-specific protein SP-B in lipid monolayers. *Biophys. J.* 81:572–585.
 79. Kandasamy, S. K., and R. G. Larson. 2005. Molecular dynamics study of the lung surfactant peptide SP-B_{1–25} with DPPC monolayers: insights into interactions and peptide position and orientation. *Biophys. J.* 88:1577–1592.
 80. Lee, H., S. K. Kandasamy, and R. G. Larson. 2005. Molecular dynamics simulations of the anchoring and tilting of the lung-surfactant peptide SP-B_{1–25} in palmitic acid monolayers. *Biophys. J.* 89:3807–3821.
 81. Choe, S., and S. X. Sun. 2005. The elasticity of α -helices. *J. Chem. Phys.* 122:244912.
 82. Ryan, M. A., X. Qi, A. G. Serrano, M. Ikegami, J. Perez-Gil, J. Johansson, and T. E. Weaver. 2005. Mapping and analysis of the lytic and fusogenic domains of surfactant protein B. *Biochemistry*. 44:861–872.
 83. Qiao, R., A. P. Roberts, A. S. Mount, S. J. Klaine, and P. C. Ke. 2007. Translocation of C₆₀ and its derivatives across a lipid bilayer. *Nano Lett.* 7:614–619.
 84. Cruz, A., C. Casals, and J. Perez-Gil. 1995. Conformational flexibility of pulmonary surfactant proteins SP-B and SP-C, studied in aqueous organic solvents. *Biochim. Biophys. Acta.* 1225:68–76.
 85. Cruz, A., C. Casals, K. M. W. Keough, and J. Perez-Gil. 1997. Different modes of interaction of pulmonary surfactant protein SP-B in phosphatidylcholine bilayers. *Biochem. J.* 327:133–138.
 86. Cruz, A., C. Casals, I. Plasencia, D. Marsh, and J. Perez-Gil. 1998. Depth profiles of pulmonary surfactant protein B in phosphatidylcholine bilayers, studied by fluorescence and electron spin resonance spectroscopy. *Biochemistry*. 37:9488–9496.
 87. Shanmukh, S., P. Howell, J. E. Baatz, and R. A. Dluhy. 2002. Effect of hydrophobic surfactant proteins SP-B and SP-C on phospholipid monolayers. Protein structure studied using 2D IR and β_v correlation analysis. *Biophys. J.* 83:2126–2141.